Journal of Materials Chemistry C

ROYAL SOCIETY OF CHEMISTRY

PAPER

Check for updates

Donor position driven excited state modulation in benzoylthiophene–carbazole emitters: divergent TTA/RTP pathways for high efficiency blue-cyan OLEDs

Ajeet Kumar Sharma,†[a] Prasannamani Govindharaj,†[b] K. R. Justin Thomas [ID] *[a] and Przemyslaw Data [ID] *[b]

Positional isomerism offers a powerful strategy for regulating emissive pathways in organic luminophores, enabling access to room-temperature phosphorescence (RTP), aggregation-induced emission (AIE), triplet–triplet annihilation (TTA), dual emission, and through-space charge transfer (TSCT). Despite these advances, a systematic understanding of positional effects in donor–acceptor (D–A) systems capable of supporting both RTP and TTA remains limited. Herein, three D–A positional isomers (**4a–4c**) are designed by anchoring *N*-phenylcarbazole at the C3, C4, and C5 positions of thiophene within a benzoylthiophene scaffold, where the benzoyl group is fixed at the C2 position. This regio-modulation induces pronounced variations in molecular conformation, electronic structure, and excited-state dynamics, as revealed by combined experimental studies and density functional theory calculations. All isomers exhibit AIE behaviour, with progressively enhanced emission from the 2,5-isomer (**4a**) to the 2,3-isomer (**4c**), driven by increasing restriction of intramolecular rotation. The 2,4-isomer (**4b**) displays dual locally excited (LE) and charge-transfer (CT) emission in toluene/DCM mixtures, whereas **4c** exhibits TSCT emission arising from a large donor–acceptor dihedral angle. All compounds show RTP, while **4b** and **4c** further demonstrate temperature-induced non-classical dynamic RTP associated with twisted triplet states. Owing to relatively large ΔE_{ST} values, reverse intersystem crossing is inefficient, suppressing TADF, and the delayed emission originates predominantly from RTP and/or rapid TTA. OLEDs based on these emitters produce deep blue to cyan electroluminescence, with the **4b**-based device achieving a maximum EQE of 17%. Overall, this work establishes donor positional control as an effective molecular handle for tuning LE–CT balance and triplet utilization in organic emitters.

[a] *Organic Materials Laboratory, Department of Chemistry, Indian Institute of Technology Roorkee, Roorkee – 247667, India. E-mail: krjt@cy.iitr.ac.in*

[b] *Department of Molecular Physics, Faculty of Chemistry, Łódź University of Technology, 90-543 Łódź, Poland. E-mail: przemyslaw.data@p.lodz.pl*

† These authors contributed equally to this work.

1. Introduction

Organic π-conjugated fluorophores are crucial for advancing organic electronic devices like organic light emitting diodes (OLEDs),[1–3] organic photovoltaics (OPVs),[4,5] nonlinear optics (NLO)[6,7] and sensors[8] due to their tuneable optical and electronic properties. Among various device types, OLEDs stand out for their practical applications in lighting and displays. While organic fluorophores come in forms such as small molecules,[9,10] dendrimers[11] and polymers,[12] small molecules are highly favoured in OLEDs, offering precise structural control and allowing their properties to be readily tailored through straightforward chemical tuning. Especially in OLED design, small-molecule donor–acceptor (D–A) fluorophores have become promising by delivering adjustable emission, efficient charge balance, and robust thermal stability, enabling finely optimized device performance.[13,14] According to the spin statistics, the proportion of singlet and triplet excitons is 1 : 3 under electrical excitation.[15] Achieving 100% internal quantum efficiency (IQE) requires harvesting both singlet and triplet excitons. This can be accomplished using either phosphorescent emitters or delayed fluorescent (DF) emitters. DF emitters are further divided into two categories: (1) E-type, corresponding to thermally activated delayed fluorescence (TADF), and (2) P-type, based on triplet–triplet annihilation (TTA). Phosphorescent OLEDs achieve 100% IQE *via* strong spin–orbital coupling (SOC) incorporating heavy metal (such as platinum and iridium) or heavy atom (such as O and S) effects.[16] To harvest

This journal is © The Royal Society of Chemistry 2026

J. Mater. Chem. C, 2026, **14**, 7451–7465 | 7451

triplet excitons, TADF effectively converts triplet excitons into singlet *via* reverse intersystem crossing (RISC) to achieve 100% IQE, while TTA is a unique phenomenon that converts two triplet excitons to one singlet exciton with higher energy. So, TTA can provide a theoretical maximum IQE of 62.5% and is widely observed in molecules featuring polyaromatic extended conjugation.[17] Among the different types of organic luminogens, ketone-based acceptor containing molecules have attracted much attention of researchers due to their n–π* transition leading to an increase in SOC, which enhances RISC efficiency, and improved stability compared to other traditional systems like phosphine oxides and sulfone-based materials.[18–20] Several researchers focused on ketone derivatives due to their TADF, room-temperature phosphorescence (RTP) and TTA properties.[21] Adachi and coworkers developed anthraquinone-based TADF emitters with prominent intramolecular charge transfer.[22] Bryce and co-workers reported a D–A type RTP compound containing phenothiazine as the donor and benzophenone as the acceptor.[23] The Congreve group demonstrated diketopyrrolopyrroles as triplet fusion upconversion materials.[24] Positional heterogeneity offers an effective molecular strategy for controlling excited-state behaviour by enabling fine adjustment of electronic interactions within a constant molecular scaffold. Shifting the relative positions of donor and acceptor units alters orbital communication, charge-transfer strength, and spin-related transition probabilities, thereby influencing intersystem crossing and triplet stabilization. Importantly, these effects are achieved through spatial reorganization alone, allowing excited-state dynamics to be tuned without any change in chemical composition.[25] Recent studies have demonstrated that positional and constitutional isomerism can profoundly regulate molecular packing, excited-state character, and optoelectronic performance, even in chemically identical frameworks. The Rajneesh group reported D–A positional isomers based on benzothiazole and phenothiazine, and their intrinsically twisted, non-planar structures endow them with AIE characteristics.[26] Several D–A positional isomers have been intensively studied and found to exhibit tuneable aggregation-induced emission (AIE).[27–29] In these compounds, the non-planar framework suppresses π–π stacking and, through the restriction of intramolecular rotation (RIR), leads to enhanced emission in the aggregated state.

Generally, RTP and through-space charge transfer (TSCT) properties depend on the orientation of the donor and acceptor moieties. Since the molecular conformations play a critical role in the RTP behaviour of organic emitters, positional isomers have also been employed to explore RTP behaviour. The Li group introduced dioxaborolane substituents at the *ortho*-, *meta*-, and *para*-positions of a benzophenone phenyl ring and investigated RTP properties. Notably, the *para*-substituted isomer exhibited polymorph-dependent emission and long-lived RTP (17.1 ms), attributed to the effective p–π conjugation between the boron atom (bearing an empty p-orbital) and the phenyl group.[30] The Zhao group introduced a carbazole unit at the *ortho*-position of the benzophenone phenyl ring, enabling two-photon excited ultralong organic room-temperature

phosphorescence (TPUOP) through enhanced charge-transfer character arising from through-space interactions.[31] Furthermore, the small energy gap enables dual-channel triplet harvesting *via* ultralong TADF and H-aggregate phosphorescence, effectively suppressing triplet–triplet concentration quenching. Positional isomers can also promote TSCT by enabling close stacking between donor and acceptor units within rigid heteroaromatic frameworks. The Ren group reported TSCT–TADF compounds in which TSCT effectively accelerates the radiative transition of singlet excitons.[32] The reduced vibrational relaxation in both the ground and excited states lead to a smaller Stokes shift, resulting in characteristically narrow emission. Despite substantial advances in realizing RTP in organic emitters, the underlying design principles remain poorly defined, primarily owing to the limited understanding of how molecular structure governs RTP-related photophysical processes.

Further dual-emissive organic emitters have drawn significant attention in white OLEDs,[33] chemosensing,[34] bioimaging[35] and mechanoresponsive[36] materials due to their potential applications. Dual emission depends on the excited state properties of the molecule, so dual emission can be generated from dual conformations/equilibrated locally excited (LE) and charge-transfer (CT)/hybrid intramolecular and intermolecular CT/multiple triplet levels/two intramolecular CTs (ICTs).[37] By increasing the effective conjugation length in D–A molecules, the hybridization of LE and CT can be observed. With the control of the donor as well as the conjugation length through steric or substituent patterns in D–A molecules, LE and CT emission can be established, which could guarantee a dual-emission characteristic at the single molecular level.[38]

The Huang group reported the design principles of D–A organic molecules to utilise the singlet–triplet exciton, aiming to achieve a small ΔE_{ST} value through bulky substituents and π-conjugation length, as well as theoretical considerations.[39] There are several D–A based benzophenone molecular designs proposed to adjust ICT and ΔE_{ST} by replacing one phenyl in benzophenone with pyridine,[40] pyrene,[41] imidazo[1,2-*a*]pyridine,[42] quinoline,[43] thiophene/furan,[44] aroylthiophene,[45] dibenzothiophene,[46,47] and *N*-phenylcarbazole.[48] In the thiophene/furan derivatives, Rajamalli and co-workers found that the direct conjugation of the heavy atom facilitates RISC and triggers TADF in the benzoyl thiophene/furan derivatives.[44] However, in these compounds, the donors were tethered through the phenyl ring. Tang and co-workers revealed that replacement of one of the phenyl groups of benzophenone with dibenzothiophene[46,47] or *N*-phenylcarbazole[48] and appending the other phenyl group with strong electron donors such as phenoxazine, phenothiazine or 9,9-dimethylacridine results in aggregation induced emissive materials with TADF properties. However, donor decoration on the heteroaromatic units in such designs has not been explored yet to the best of our knowledge.

In this work, we adopted a D–A molecular design by replacing one phenyl unit with thiophene in benzophenone (**4a**, **4b** and **4c**), employing *N*-phenylcarbazole (*N*-PhCbz) as the donor and benzoyl-thiophene as the acceptor. The donor was anchored through the thiophene nucleus substitution and the

7452 | *J. Mater. Chem. C*, 2026, **14**, 7451–7465

This journal is © The Royal Society of Chemistry 2026

positional variation of the donor on the thiophene ring enables systematic control of charge-transfer (CT) interactions and D–A torsion, which are crucial for modulating ΔE_{ST} and governing RTP/TTA behaviour. We found that the ΔE_{ST} increases as the donor is kept away from the acceptor unit on the thiophene nucleus (C3 to C5). Despite a small ΔE_{ST} observed for the isomer, **4c** possessing the donor and acceptor at proximal positions, the rate of reverse intersystem crossing (RISC) is not sufficient to realize TADF. Nevertheless, the donor introduction on the thiophene nucleus facilitates AIE, RTP and TTA. The concerted action of RTP and TTP led to a maximum external efficiency of 17% for isomer **4b** in an OLED.

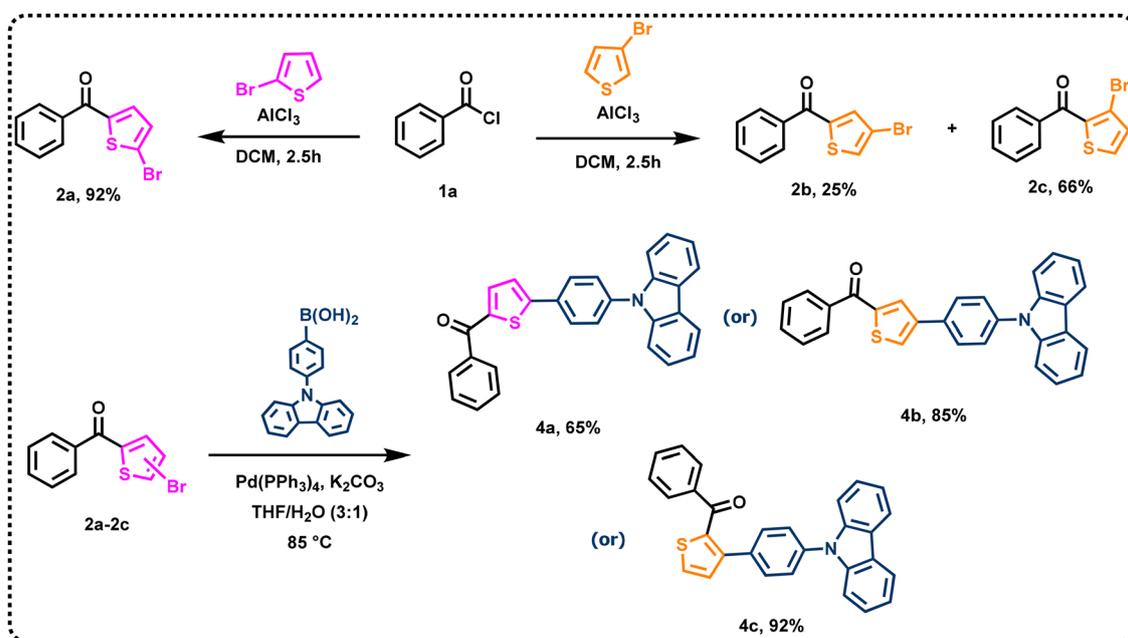## 2. Results and discussion

2.1. Synthesis and characterization

The synthetic route for preparing the three di-substituted thiophene dyes is presented in Scheme 1. The key starting materials such as (4-(9H-carbazol-9-yl)phenyl)boronic acid (3) and (5-bromothiophen-2-yl)(phenyl)methanone (**2a**) were synthesized according to literature methods.[49,50] The important intermediates (4-bromothiophen-2-yl)(phenyl)methanone (**2b**) and (3-bromothiophen-2 yl)(phenyl)methanone (**2c**) were synthesized by Friedel–Crafts acylation. Finally, intermediates **2a**, **2b** and **2c** were converted to final dyes **4a**, **4b** and **4c**, respectively, via Suzuki coupling reaction treating them with (4-(9H-carbazol-9-yl)phenyl) boronic acid (3). The structures of dyes **4a**, **4b** and **4c** were established by ^{1}H NMR, ^{13}C NMR, FTIR, and HRMS spectroscopy and elemental analyses. In addition, the molecular structures of **4a**, **4b** and **4c** were confirmed by single crystal X-ray diffraction analysis (Fig. 1). Dyes **4a**, **4b** and **4c** are light yellow, white, and light-yellow solids, respectively. All dyes are soluble in common organic solvents such as toluene (TOL), tetrahydrofuran (THF), dichloromethane (DCM), N,N-dimethylformamide (DMF), acetonitrile (ACN), trichloroethylene (TCE), and dimethyl sulphoxide (DMSO) but insoluble in alcohols.

2.2. Single crystal analysis

Single crystal XRD structures (CCDC 2516522–2516524) were used to analyse the intermolecular and intramolecular interactions in dyes **4a**, **4b**, and **4c**. The suitable crystals were obtained by crystallization induced by the layer diffusion method in a DCM–hexane mixture at room temperature. The structures are shown in Fig. 1a and b. The angles (α) between thiophene and the phenyl group of N-PhCbz were 13.75°, 22.05°, and 49.56° for **4a**, **4b**, and **4c**, respectively. The angles (β) between the phenyl group of N-PhCbz and carbazole were 53.49°, 57.59°, and 53.72° for **4a**, **4b**, and **4c**, respectively. The orientations of dyes **4a**, **4b**, and **4c** are linear to bent due to the steric interaction between the donor and the acceptor leading to changes in dihedral angles (**4a** – 13.75°, **4b** – 22.05°, and **4c** – 49.56°) as shown in Fig. 1a. These results show that dye **4c** has the potential to exhibit TADF properties due to large dihedral angles between the donor and acceptor, leading to a small ΔE_{ST} value.[51]

In dye **4a**, one carbazole unit is perpendicular and sandwiched between two other molecules due to C–H···π (phenyl of N-PhCbz and Cz) and C–H···O intermolecular interactions, with distances of 2.76 Å and 2.33 Å, respectively. In dye **4b**, two molecules are anti-parallel due to C–H···π (centroid–phenyl of benzoyl and centroid–phenyl of the benzoyl group), C–H···O, and C–H···S intermolecular interactions, with distances of 3.34 Å, 2.65 Å, and 2.94 Å, respectively. In dye **4c**, two molecules are oriented perpendicular due to C–H···π (H···centroid distance) and C–H···O intermolecular

Scheme 1 Synthetic protocol of dyes **4a**, **4b** and **4c**.

This journal is © The Royal Society of Chemistry 2026

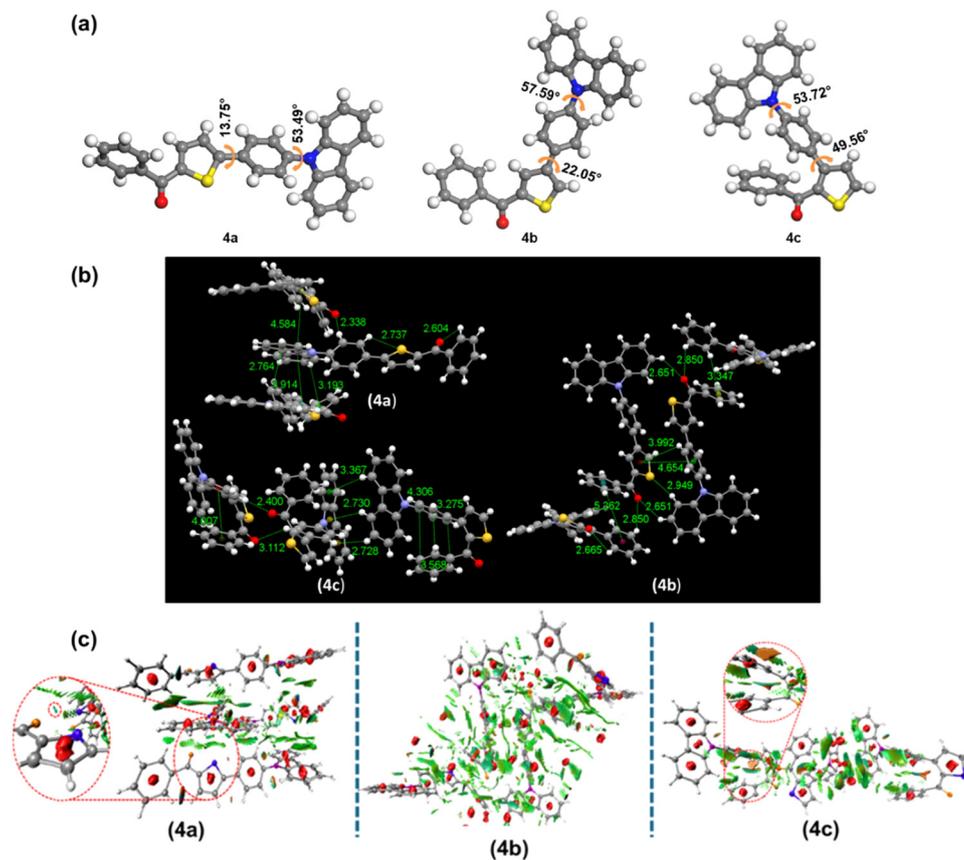J. Mater. Chem. C, 2026, **14**, 7451–7465 | **7453**

Fig. 1 (a) Dihedral angle between *N*–PhCbz (donor) and benzoyl thiophene (acceptor) in dyes **4a**, **4b** and **4c**. (b) The molecular structures of dyes **4a**, **4b** and **4c** acquired from SCXRD analysis and inter/intramolecular interactions between the molecules. (c) NCI analysis of dyes **4a**, **4b** and **4c**.

interactions, with distances of 2.73 Å and 2.40 Å, respectively. The distances between adjacent molecules were found to be 3.91 Å and 4.65 Å for dyes **4a** and **4b**, respectively. Interestingly, dye **4c** showed intramolecular distances of 3.27 Å, 3.56 Å, 4.30 Å, and 4.00 Å (centroid···centroid distance) between the phenyl of the benzoyl group and the phenyl of *N*-PhCbz, which may be responsible for through-space charge transfer.[32,52] TSCT is supported by the change in dipole moment calculated using the L–M plot, and dye **4c** showed a greater change in dipole moment compared to dye **4a**. Organic dyes contain a carbonyl group and thiophene that can be responsible for RTP. Hence, all dyes exhibit intermolecular and intramolecular C–H···X (O, S) interactions, which are taken into consideration for the persistent RTP effect due to their effective suppression of non-radiative decay.[53]

Multiwfn[54] software was used to analyse the noncovalent interaction (NCI) in the synthesized dyes, and VMD software was used to visualize the plots (Fig. 1c). Strong π–π interactions (green isosurfaces) were observed between the carbazole of *N*-PhCbz and the benzoyl thiophene of other molecules in dye **4a**, and between the phenyl of *N*-PhCbz and the thiophen unit of other molecules in dye **4b**. Interestingly, dye **4c** exhibited repulsive π–π interactions between the phenyl of benzoyl thiophene and the phenyl of *N*-PhCbz of the same molecule due to TSCT.

2.3. Theoretical analysis

To elucidate the structural impact on the photophysical properties of the positional isomers (**4a**, **4b**, and **4c**), their structures were optimized at the B3LYP/def2-svp level. TD-DFT computations were performed at the B3LYP/def2-TZVP level on the ground state optimized structures to calculate the oscillator strengths and vertical excitation energies (Fig. 2 and Fig. S15–S18). The electronic distributions on the frontier molecular orbitals of the molecules revealed the extent of charge transfer in the molecules. The highest occupied molecular orbitals (HOMOs) of the molecules were mainly located on the donor segment (*N*-PhCbz), while the lowest unoccupied molecular orbital (LUMO) is confined to the acceptor fragment (benzoyl thiophene). Interestingly, the overlapping of the HOMO and LUMO on thiophene and the phenyl of *N*-PhCbz decreased upon moving from dye **4a** to **4c** due to increasing dihedral angle (13.75° to 49.56°) between the donor and acceptor fragments. This manifested in the small ΔE_{ST} of 0.199 eV for **4c**, while dyes **4a** and **4b** possessed relatively large ΔE_{ST} of 0.309 eV and 0.481 eV, respectively. Also, the energy gap between T_1 and T_2 decreases upon moving from dye **4a** to **4c** (for **4a**, $\Delta E_{T_1-T_2}$ = 0.491 eV; for **4b**, $\Delta E_{T_1-T_2}$ = 0.315 eV, and for **4c** $\Delta E_{T_1-T_2}$ = 0.192 eV). Thus, positional isomerism not only affects the gap between the singlet and triplet states but also the relative positioning of the triplet states. To investigate all possible
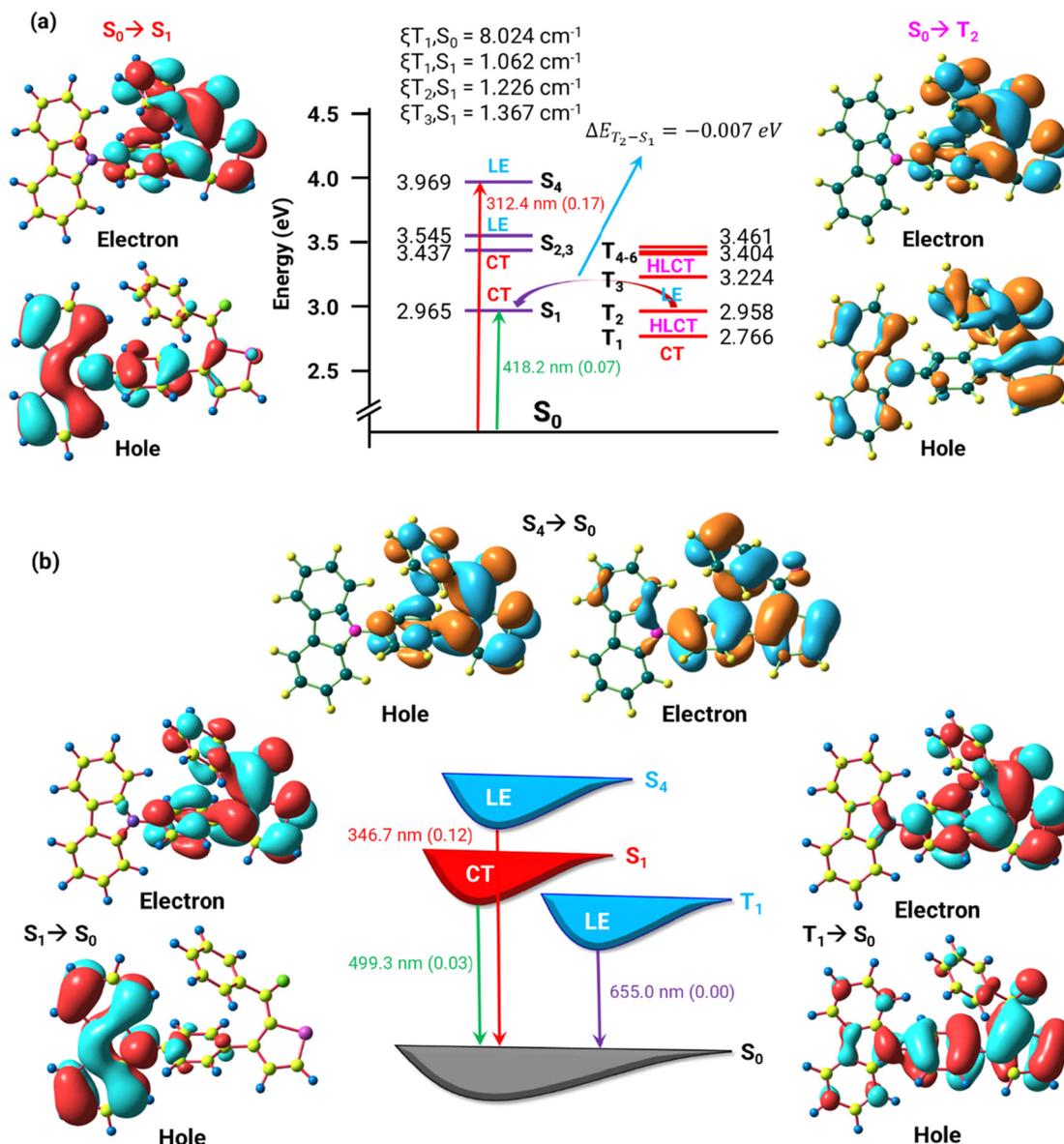
Fig. 2 (a) Energy level diagram (excitation from S_0) of **4c** and (b) NTO analysis of the emission of **4c**.

pathways of RISC, we have analysed few excited singlet and triplet states of all positional isomer dyes (**4a**, **4b** and **4c**) and a representative energy diagram and natural transition orbitals corresponding to the analysed states are illustrated in Fig. 2. In the case of dye **4a**, the S_1 state is CT and the T_1 state is HLCT in nature. The T_1 state lies below the S_1 state with a large energy gap (0.481 eV). Both T_2 and T_3 states with HLCT character lie closely to the CT dominated S_1 state resulting in a small ΔE_{ST} value (0.010 eV). This indicates the possibility of existence of a hot exciton channel for reverse intersystem crossing in this molecule. In the case of **4b**, the S_1 state is CT and the T_1 state is LE in nature. The T_1 state lies below the S_1 state with a substantial energy of 0.309 eV. However, the T_2 state with HLCT character lies close to the CT dominated S_1 state (0.006 eV), which suggests a possibility of RISC between T_2 and S_1 states.

In the case of dye **4c**, the S_1 state is CT and the T_1 state is CT in nature. The T_1 state lies below the S_1 state with a relatively small $\Delta E_{S_1 T_1}$ value (0.199 eV). However, the T_2 state of HLCT character lies almost degenerate with the S_1 state (0.007 eV). This facilitates the RISC between the T_2 and S_1 states. The decreasing T_1–T_2 gap from **4a** to **4c** reflects a gradual reordering and compression of triplet excited states induced by donor positional isomerism. In **4c**, increased donor–acceptor separation and through-space coupling stabilize higher-lying CT-like triplet states, bringing them closer in energy to the lowest triplet state. SOC matrix elements between S_1 and T_1 are 0.27, 0.74 and 1.06 cm^{-1}, respectively, for **4a**, **4b** and **4c**. This trend supports the fact that the spatial proximity of donors and acceptors enhances SOCME and reduces ΔE_{ST}. The enhanced SOCME in **4b** and **4c** can be attributed to increased orbital

This journal is © The Royal Society of Chemistry 2026

J. Mater. Chem. C, 2026, **14**, 7451–7465 | **7455**

mixing between LE and CT states, which facilitates spin–orbit coupling. In all compounds, the T_2 state is aligned close to S_1. The corresponding SOCME values between the T_2 and S_1 states of compounds **4a**, **4b** and **4c** are 2.56, 3.34 and 1.23 cm^{-1}, respectively. These moderate SOCME values observed for all three isomers (**4a**–**4c**) may facilitate the spin-flipping of triplet excitons from the T_2 state to the S_1 state and accelerate RISC. Compound **4c** exhibits pronounced TSCT character arising from its large donor–acceptor dihedral angle, which limits through-bond conjugation while enabling through-space electronic interactions. NTO analysis of the $S_0 \rightarrow S_1$ transition reveals spatially separated hole and electron distributions (Fig. 2a), consistent with negligible through-bond overlap and TSCT excitation. This electronic configuration underpins the unique emission features of **4c** and accounts for the reduced exchange interaction, resulting in a small ΔE_{ST}.

2.4. Thermal properties

All dyes exhibited excellent thermal stability with high thermal decomposition temperature (T_d) in the range of 350–450 °C. The onset decomposition temperatures corresponding to the 5% weight loss (T_{onset}) are above 350 °C (Fig. 3a). Since dyes **4a**, **4b** and **4c** possess the same molecular weight, the difference in thermal stability may arise from the variations in geometrical orientations. It is probable that in **4a**, a more planar arrangement between benzoyl and N-phenyl carbazole units helps to achieve an ordered structure in the solid state. The compounds containing planar fragments have been reported to exhibit pronounced thermal stability.[55–57] The glass transition temperatures of the dyes measured from differential scanning calorimetry studies were low < 65 °C (Fig. 3b and Fig. S14), confirming their crystalline nature.

2.5. Photophysical properties

The photophysical properties of all dyes were investigated by UV-visible absorption and fluorescence spectroscopy. The absorption spectra of the compounds recorded in DCM are displayed in Fig. 4 and the relevant data are compiled in Table 1. All compounds showed three prominent absorption peaks in the range 230–370 nm. The shorter wavelength absorbance band observed below $\sim$300 nm is assigned to the multiple localized π–π^* and n–π^* electronic transitions originating from chromophores benzoylthiophene and N-phenyl-carbazole. The longer wavelength absorption band appearing in the wavelength range 340–370 nm is invariably present in all compounds and assigned to the intramolecular charge transfer transition from N-phenyl carbazole to benzoyl thiophene. Moreover, the position of chromophores on thiophene with respect to the benzoyl group exhibited significant influence on the absorption wavelength and molar absorption coefficients of the dyes. Interestingly, positional isomer **4a** displayed a bathochromic shift in absorption, which is attributed to the linear conjugation of N-phenyl carbazole with respect to the benzoyl group on thiophene. The molar absorption coefficient for the longer wavelength absorption in these dyes assumes the order **4a** > **4b** > **4c**, which is analogous to the increase in the dihedral angle between the donor and acceptor and inhibited electronic delocalization on increasing the twisting between the chromophores.

The emission spectra of the compounds recorded in DCM are shown in Fig. 4(b) and the corresponding data are listed in Table 1. Interestingly, dyes **4a**, **4b** and **4c** showed similar emission profiles, indicating that the emission originates from a similar electronic state. Since all dyes possess benzoyl and N-phenylcarbazole units, it is speculated that the emission originates from the ICT state involving these two chromophores.

Furthermore, to understand the interaction of dyes with solvents in ground and excited states, a solvatochromic study was performed with different solvents. The absorption and emission spectral variations observed due to solvent polarity are displayed in Fig. 4, Fig. S2–S4 and Tables S2–S4. It is observed that all compounds display solvent-insensitive absorption spectra, suggestive of a non-polar ground state. However, in the emission spectra, the compounds exhibit positive solvatochromism, *i.e.*, the emission maxima progressively increase on increasing solvent polarity (Fig. 5 and Fig. S2–S4). This allows us to make a conclusion that these dyes are selectively stabilized by polar solvents in the excited
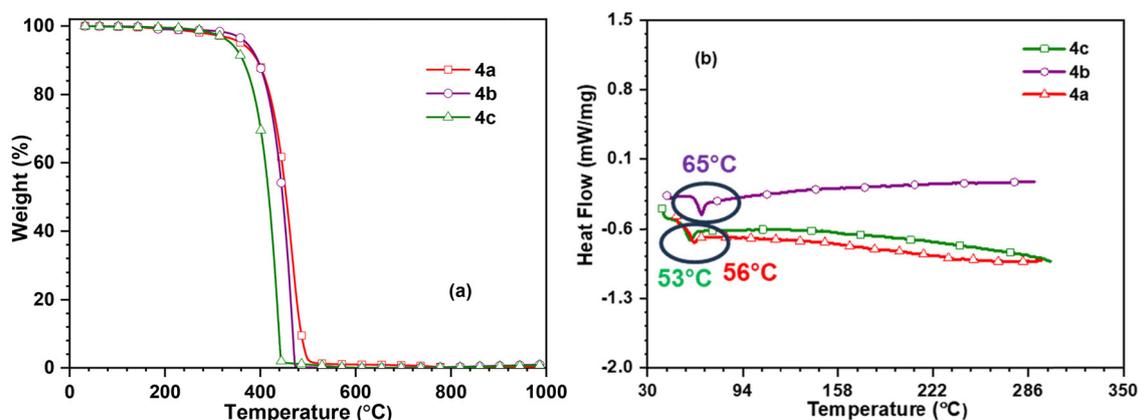

Fig. 3 (a) Thermogravimetric plots of dyes **4a**, **4b** and **4c**. (b) DSC traces of **4a**, **4b** and **4c**.
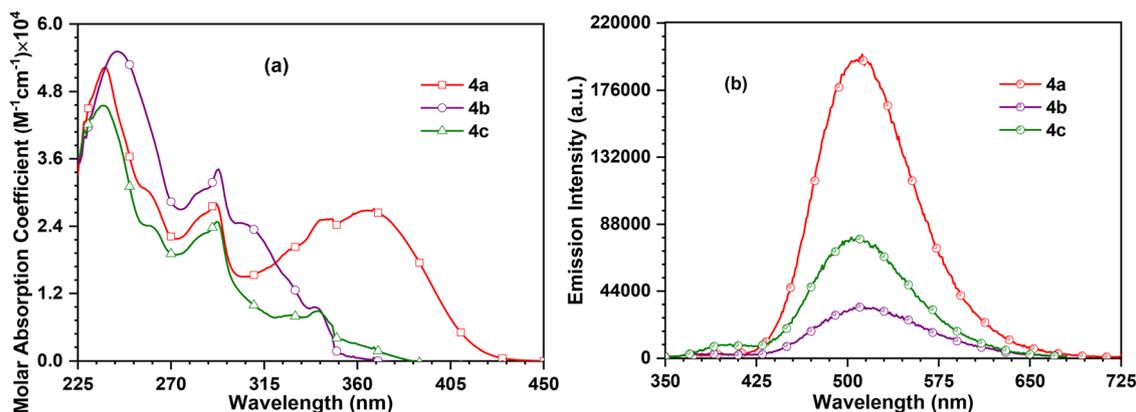
7456 | *J. Mater. Chem. C*, 2026, **14**, 7451–7465

This journal is © The Royal Society of Chemistry 2026

Fig. 4 (a) Absorption and (b) emission spectra of the dyes recorded in 1×10^{-4} M and 1×10^{-5} M DCM solutions, respectively.

Table 1 Optical properties of the dyes

Dye	$\lambda_{abs}{}^a$ [nm] ($\varepsilon_{max} \times 10^4$ [M^{-1} cm^{-1}])	$\lambda_{em}{}^a$ [nm] (Φ_f, % (sol/film))[b]	Stokes shift [cm^{-1}]	$\lambda_{em}{}^c$ [nm]	$\Delta\mu^d$ [Debye]
4a	367 (2.7), 292 (2.79), 237 (5.23)	509 (11, 13)	7714.5	492	11.77
4b	305 (2.42), 292 (3.40), 245 (5.53)	391, 510 (15, 19)	13 369.4	451	16.89
4c	342 (0.87), 292 (2.49), 237 (4.56)	505 (9, 14)	9523.5	441	15.23

[a] Measured in DCM solution. [b] Absolute quantum yields determined using a calibrated integrated sphere system. [c] Measured for drop-cast films from toluene. [d] Calculated from Lippert–Mataga analysis.

state due to enhanced polarization.[46,58] Emission shifts to longer wavelengths in these dyes in polar solvents may arise due to the following reasons: (a) structural reorganization due to solvation effects and/or (b) stabilization in polar solvents due to photo-induced intramolecular charge transfer (ICT). This is further confirmed by comparing the Stokes shifts of the compounds in non-polar (Hex) and polar (DMSO) solvents. The estimated emission shift ($\Delta\lambda$) between these solvents (λ_{DMSO}–λ_{Hex}) for dyes lies in the range of 117–187 nm and assumes the order **4b** (187 nm) > **4c** (152 nm) > **4a** (117 nm). The large Stokes shift and the decrease of quantum yield in polar solvents cannot originate from structural changes alone, ICT may be the reason for poor quantum yields.[59,60] Dye **4b** displayed dual emission spectra due to locally excited (LE) and charge transfer (CT) states. The LE and CT character of dye **4b** was analysed using a toluene–dichloromethane binary solvent system (Fig. 5b and Fig. S5). The emission from the CT state is pronounced upon increasing the DCM content. Since the compounds showed positive solvent-dependent emission properties, we attempted to evolve the correlation of Stokes shift with orientation polarizability (Fig. 5c). The dyes showed linear trends with positive slopes, which indicated a general dye–solvent interaction in the excited state.[38] The slope for dye **4c** is relatively large, supporting the above observations.

The emission spectra recorded for the drop-cast thin films of all dyes (**4a**, **4b** and **4c**) are displayed in Fig. 5d. The compounds in thin film exhibited a broad emission spectrum in close agreement with those observed in toluene solutions. This probably indicates that the dielectric constants for the solid films of the dyes are approximately close to those observed in corresponding toluene solutions.

2.6. Aggregation-induced emission

To understand the solid-state emission behaviour of dyes **4a**, **4b** and **4c**, we performed aggregation studies in a THF–water binary solvent mixture (Fig. 6). Dye **4a** showed a decrease of emission intensity upon increasing the water fraction (f_w) from 0% to 50% due to amorphous morphology.[61] Upon further addition of water, the emission intensity of dye **4a** increased and reached maximum at 99% with a hypsochromic shift (blue shift) due to more ordered morphology. However, the intensity did not increase more than that of 0% water. However, dyes **4b** and **4c** showed noticeable AIE upon increasing the water fraction up to 90% in THF. Relatively, dye **4c** showed high AIE as compared to **4a** and **4b** due to RIR governed by a twisted structure. Dyes **4a**, **4b** and **4c** showed rod, rod and cubic morphology at 90% f_w, respectively (Fig. 6b). The hypsochromic shift in emission can be attributed due to the more crystalline rod–cubic shape, which is supported by scanning electron microscopy (SEM) images.[47,61–63]

2.7. Time-resolved photophysics

An initial steady-state photoluminescence study under degassed conditions revealed the presence of delayed emission (DE) in all three isomers (Fig. S12). To confirm this finding more deeply, time-resolved photoluminescence (TRPL) measurements were performed to elucidate the underlying complex photophysical processes. To explore the effect of the *N*-PhCbz donor substituent's position relative to the acceptor core on delayed emission dynamics, thin films were prepared by dispersing the isomers in two distinct host materials: the non-polar polymeric host Zeonex and the polar small-molecule host CBP. Solid-state
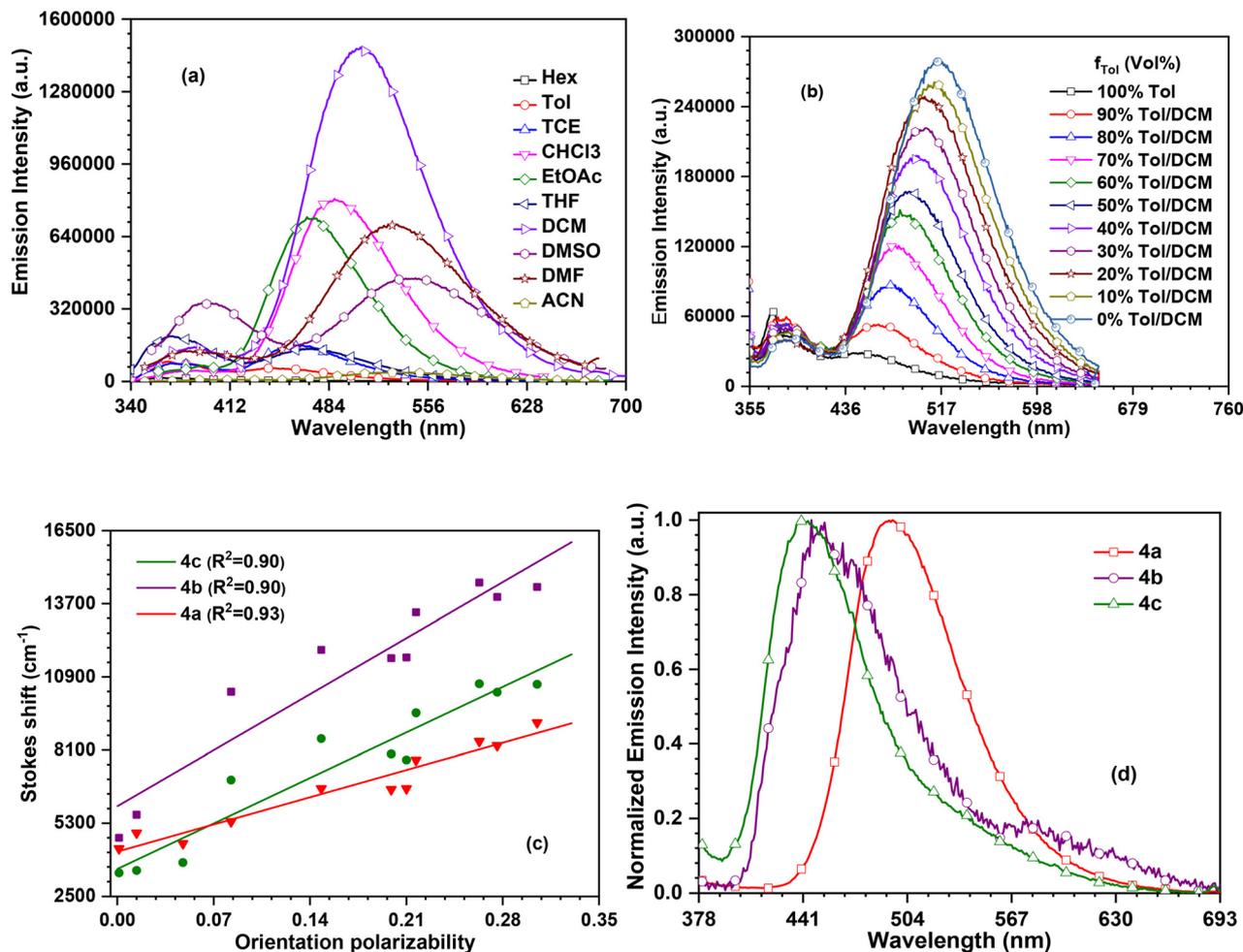
Fig. 5 (a) Emission spectra of dye **4b** recorded in different solvents. (b) Emission spectra of dye **4b** recorded in toluene/DCM solvents. (c) Plots of Stokes shift *versus* orientation polarizability. (d) Emission spectra of the drop-cast thin films of the dyes.

photoluminescence studies of the isomers revealed a significant redshift in emissions when doped in CBP compared to Zeonex (Fig. S11a and b). This spectral shift reveals the mixed character of charge-transfer (CT) and locally excited (LE) states. Although all three isomers exhibited delayed emission (DF and/or RTP), their photophysical processes differ dramatically depending on the host environment (Fig. 7), emphasizing the impact of the matrix on excited-state dynamics.

TRPL measurements of a blended film (1 wt% emitter in Zeonex) at 300 K revealed a two-component emission: prompt fluorescence (PF) from the S_1 state occurring on the nanosecond (ns) timescale and RTP from the T_1 state on the millisecond (ms) timescale (Fig. 7d–f). Notably, all three isomers exhibit stronger RTP in Zeonex than CBP, indicating that the triplet state is more stabilized in a less polar and rigid environment. This stabilization minimizes non-radiative decay to the singlet ground state (S_0), enhancing stronger RTP emission. The observed RTP, which correlates well with temperature variations (from 10 K to 300 K), suggests classical RTP from the T_1 state (Fig. S13). Additionally, the stabilization of the CT state is evident from PF spectra at 300 K (Fig. S11 and blue line

in Fig. 7a–c) and triplet emission at 10 K (10 K PH) (green line in Fig. 7a–c). This stabilization increases progressively from **4a** to **4c**.

The experimentally determined ΔE_{ST} values are 0.76 eV, 0.34 eV, and 0.28 eV for **4a**, **4b**, and **4c**, respectively, demonstrating that the positioning of the N-PhCbz donor relative to the acceptor plays a crucial role in reducing ΔE_{ST} (Table 2). However, despite this reduction, the lowest ΔE_{ST} achieved (0.28 eV) remains insufficient to facilitate TADF. Consequently, only substantial RTP is observed in Zeonex, without any trace of DF (Fig. 7).

The TRPL analysis of a 10 wt% emitter in the OLED matrix, 4,4′-bis(N-carbazolyl)-1,1′-biphenyl (CBP), revealed more complex excited-state dynamics due to the presence of multichannel triplet emissions. Unlike in Zeonex, each isomer exhibited entirely different behaviour in the CBP host. For **4a**, three distinct emission components were observed: PF, DF, and RTP (Fig. 8a and d). The DF component in **4a** likely originates from triplet–triplet annihilation rather than TADF, as the ΔE_{ST} value (>0.3 eV) is too large to upconvert the triplet exciton through RISC to achieve efficient TADF. At the beginning of the

7458 | *J. Mater. Chem. C*, 2026, **14**, 7451–7465

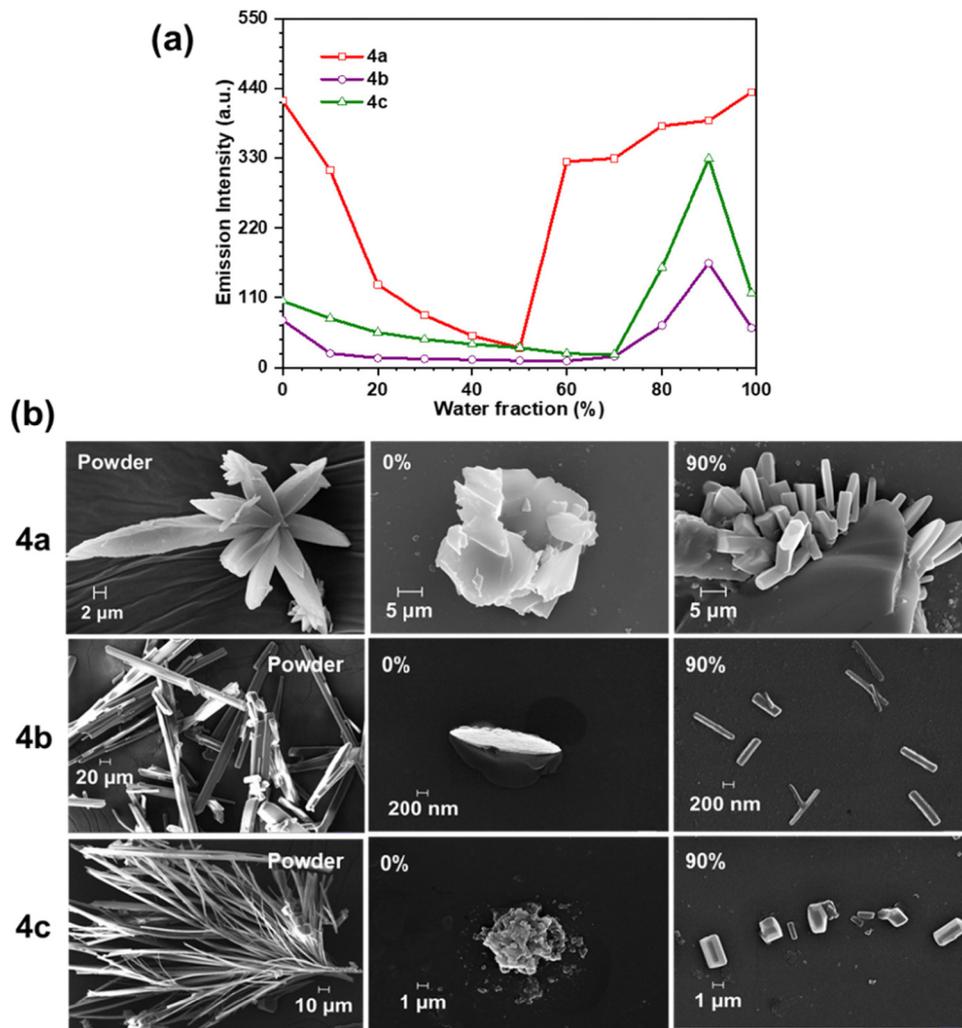This journal is © The Royal Society of Chemistry 2026

Fig. 6 (a) Aggregation studies of dyes **4a**, **4b** and **4c** in a THF : water mixture, (b) SEM images of dyes **4a**, **4b** and **4c** in powder and aggregated forms obtained from different water ratios.

ms range ($\sim$2 ms), **4a** displayed a combination of TTA and RTP (green line in Fig. 8a). However, with longer delays, TTA was completely overshadowed by strong RTP. Notably, the 10 K phosphorescence (PH) spectrum of **4a** perfectly overlapped with its 300 K RTP spectrum at 6 ms, confirming that **4a** exhibits classical RTP from the T_1 state. This behaviour can be attributed to the linear conjugation between the donor and acceptor, which prevents other conformations that lead to twisted intramolecular charge transfer (TICT) and/or TSCT.

Similarly, **4b** also exhibited two delayed components: DF in the ms range and RTP in the ms range. Similarly to **4a**, **4b** displayed a distinct DF component, likely arising from TTA rather than TADF, even with its lower ΔE_{ST}. This is mostly because of the lack of temperature impact on the change of intensity. Interestingly, the 300 K PH spectrum (at 4 ms, purple colour in Fig. 8b) appeared at 627 nm, nearly 100 nm redshifted from its 10 K PH spectrum (528 nm) (red colour in Fig. 8b). This gradual red shift, observed as the temperature increased from 10 K to 300 K, suggests a unique non-classical

RTP mechanism.[64–68] This phenomenon, termed thermally stimulated dynamic organic phosphorescence (TSDOP), denoted as RTP* for clarity, arises from a TICT state. The twisting motion of the emitter is triggered as the molecule is heated gradually, leading to a structural change that enables phosphorescence even at room temperature. Typically, such emissions are not observed without molecular motion, but here in **4b** in CBP, thermal energy facilitates the transition to a conformation that enhances phosphorescence emission (Fig. 9a and b). In contrast, **4c** exhibited both TTA emission and classical RTP, along with non-classical RTP* at 50 µs. Like **4b**, a spectral red shift was also observed, but it did not follow a gradual red shift corresponding to the temperature increase (Fig. 9c). This suggests that in **4c**, a strong TSCT dominates over the TICT, leading to only a small red shift in the PH spectrum at 300 K. This unique behaviour, exclusive to **4c**, aligns well with single-crystal analysis (*vide supra*). Notably, both **4b** and **4c** involve multichannel charge-transfer triplet emission from TICT and/or TSCT states, which significantly lowers the ΔE_{ST}.
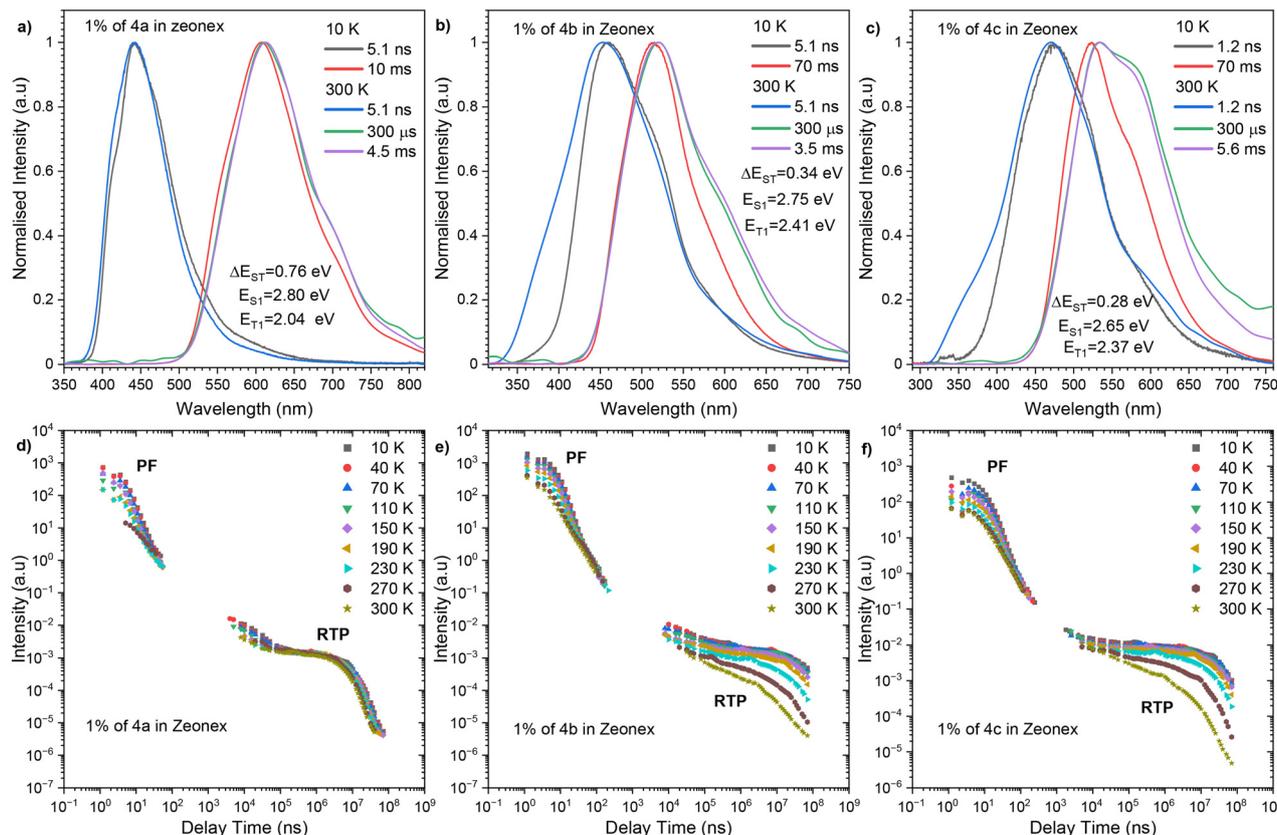
Fig. 7 Time-resolved PL spectra (a)–(c) and decay profiles (intensity *vs.* delay time) (d)–(f) of **4a–4c** in Zeonex®. The energies correspond to the maximum emission peaks and λ_{ex} = 355 nm.

Table 2 Summary of the general photophysical properties obtained from time-resolved spectra

Emitter	$\lambda_{em}{}^a$ [nm]	Host	$\Phi_{PL}{}^b$ (%)	$\tau_{PF}{}^c$ [ns]	$\tau_{DF}{}^d$ [ms]	$\tau_{RTP}{}^e$ [ms]	DE/PF^f	S$_1{}^g$ [eV]	T$_1{}^g$ [eV]	$\Delta E_{ST}{}^h$ [eV]
4a	443	Zeonex	2.8	2.54 ± 0.13	—	3.37 ± 0.42	17.81	2.80	2.04	0.76
	470	CBP	38	4.74 ± 0.14	260.940 ± 20.75	2.48 ± 0.42	3.25	2.64	2.04	0.60
4b	451	Zeonex	0.4	2.91 ± 0.25	—	2.49 ± 0.2	2.13	2.75	2.41	0.34
	460	CBP	81	5.88 ± 0.45	1.08 ± 0.09	3.3 ± 0.24	0.61	2.69	2.49	0.21
4c	468	Zeonex	0.2	7.27 ± 0.31	—	4.86 ± 0.07	14.83	2.65	2.37	0.28
	470	CBP	3.1	6.66 ± 0.54	56.9 ± 3.09	0.76 ± 0.07	9.95	2.63	2.48	0.15

^{a} The maximum wavelength (λ_{max}) of PL spectra. ^{b} Photoluminescence quantum yield in the host material, measured under ambient conditions. ^{c} Prompt fluorescence (PF) lifetime. ^{d} Delayed fluorescence (DF) lifetime. ^{e} Room temperature phosphorescence (RTP) lifetime. ^{f} The ratio of delayed emission (both DF and RTP) to prompt fluorescence (PF). ^{g} Singlet (S$_1$) and triplet (T$_1$) energy. Error ± 0.03 eV. ^{h} Energy splitting. Error ± 0.05 eV. All parameters are estimated at 300 K except the T$_1$ energy level, which was extracted from 10 K PH spectra.

Interestingly, ΔE_{ST} decreases progressively as *N*-PhCbz moves closer to the benzoyl carbonyl functional group, demonstrating that the positioning of *N*-PhCbz plays a key role in reducing ΔE_{ST} and consequently enhancing a very fast TTA process.

Comparing emission behaviour in various host matrices reveals another significant tendency; each isomer demonstrates a consistent ΔE_{ST} reduction of 0.13 eV when the host is switched from Zeonex to CBP, calculated as ΔE_{ST} (Zeonex) − ΔE_{ST} (CBP). This discovery implies that the energy gap tendency remains consistent across all isomers, despite variations in emission properties and emitter structure. This uniform shift underscores the substantial impact of the host environment

and regioisomerism on ΔE_{ST} modulation and offers valuable insight into the underlying photophysical behaviour in an excited state.

2.8. OLED performance

Finally, the OLED devices were fabricated and analysed. As shown in Fig. 10, the optimal device configuration for all compounds was found to be: indium tin oxide (ITO) as the anode, 1,4,5,8,9,11-hexaazatriphenylenehexacarbonitrile (HAT-CN), as the hole-transport layer (10 nm)/*N*,*N*'-di(1-naphthyl)-*N*,*N*'-diphenyl-(1,1'-biphenyl)-4,4'-diamine (NPB, 30 nm) as the exciton blocking layer and 10% of **4a**, **4b**, or **4c** in CBP (30 nm)/
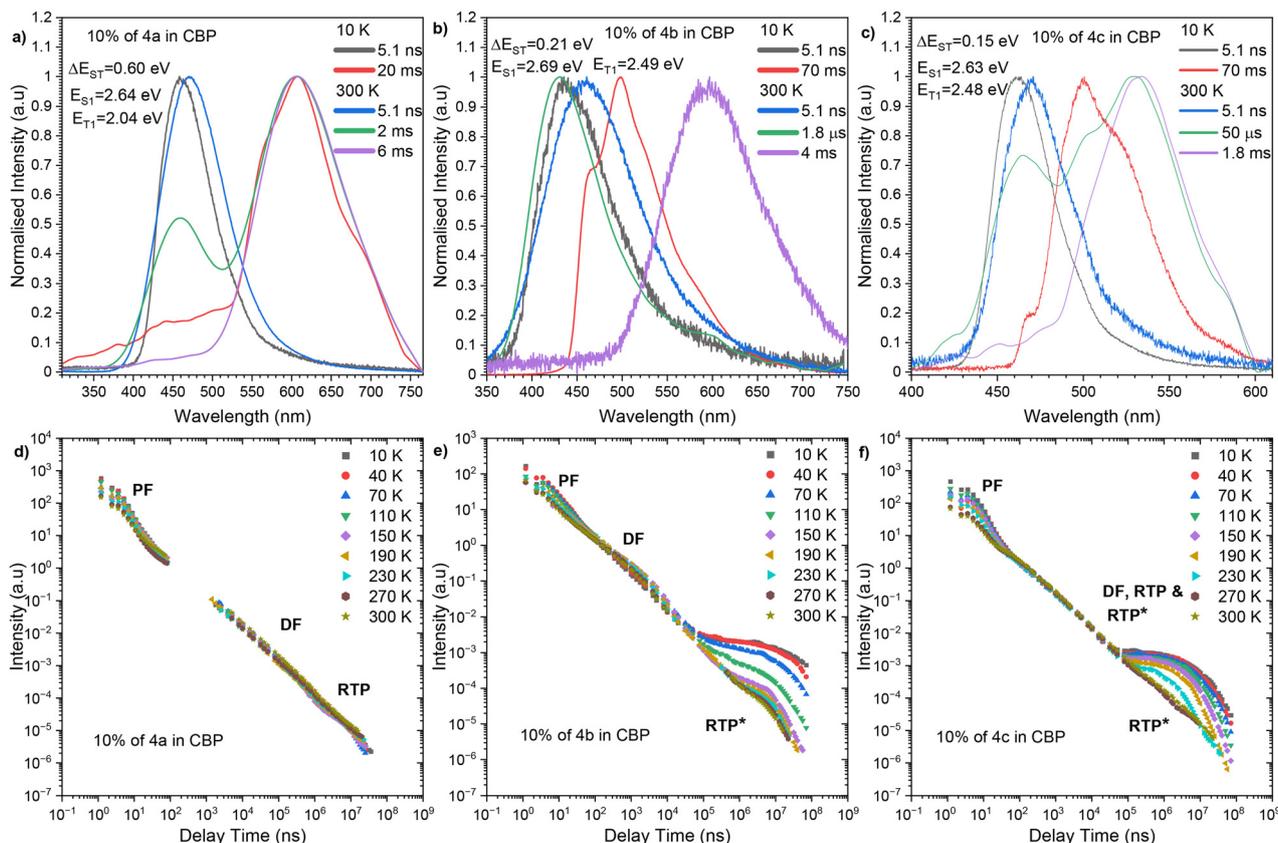
7460 | *J. Mater. Chem. C*, 2026, **14**, 7451–7465

This journal is © The Royal Society of Chemistry 2026

Fig. 8 Time-resolved PL spectra (a)–(c) and decay profiles (intensity *vs.* delay time) (d)–(f) of **4a–4c** in CBP. The energies correspond to the maximum emission peaks and λ_{ex} = 355 nm. RTP* represents the room temperature phosphorescence from the twisted conformation.
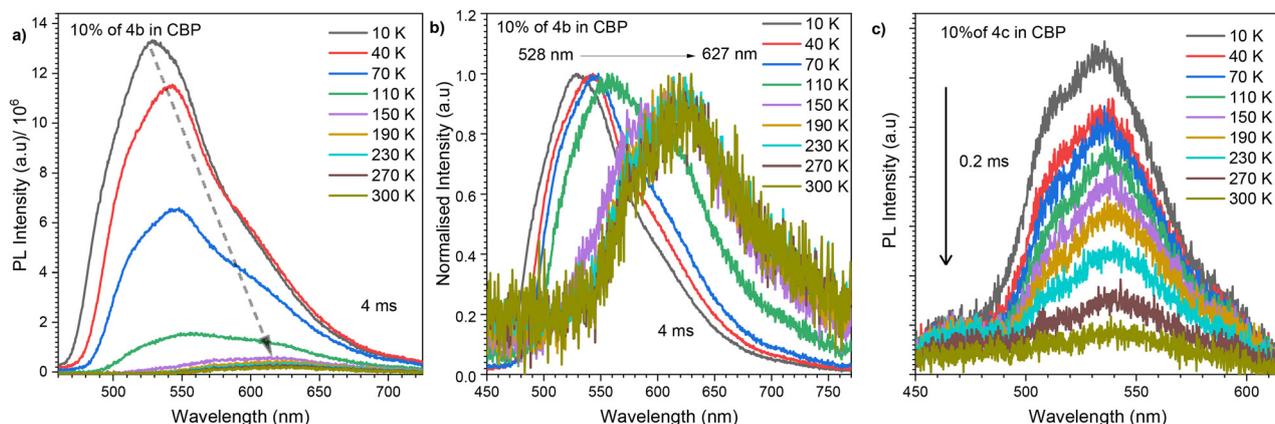

Fig. 9 Temperature-dependent time-resolved PH spectra: intensity variation of the PH spectra of 10% **4b** in CBP (a); spectral shift of the PH spectra of 10% **4b** in CBP, with respect to temperature (b); intensity variation of the PH emission of 10% **4c** in CBP (c). (a) and (b) were recorded with a delay time of 4 ms, whereas (c) was recorded with a delay time of 0.2 ms; λ_{ex} = 355 nm.

1,3,5-tri(*m*-pyridin-3-ylphenyl)benzene (TmPyPB) (40 nm) as the electron transport layer and LiF (1 nm), which alters the work function of the Al cathode (100 nm). The electroluminescence (EL) spectra reveal that each isomer exhibits distinct emission profiles, corresponding to their inherent photophysical properties and molecular conformations. Devices reach maximum

EQEs of 11.09% (**4a**), 16.96% (**4b**), and 1.28% (**4c**), with the corresponding maximum luminance values of 23 109 cd m^{-2} (**4a**), 55 338 cd m^{-2} (**4b**), and 4182 cd m^{-2} (**4c**); the EQE roll-off is smallest for **4b** and most severe for **4c**. These trends track the EL spectra and CIE coordinates shown in Fig. 10 and confirm that **4b** delivers the most balanced device operation in this
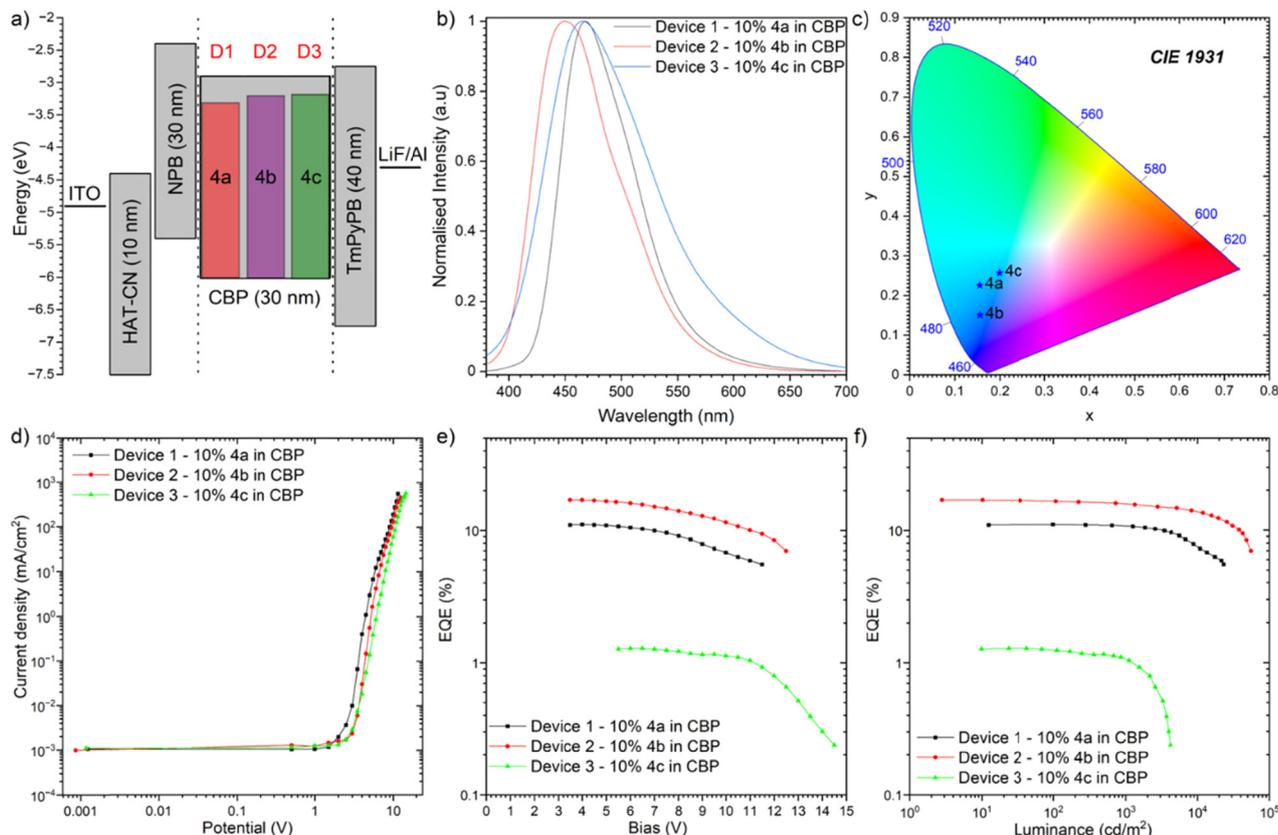
This journal is © The Royal Society of Chemistry 2026

J. Mater. Chem. C, 2026, **14**, 7451–7465 | **7461**

Fig. 10 The characteristics of the OLED devices: (a) device configuration; (b) electroluminescence spectra; (c) CIE diagram of emission colours; (d) current density–bias characteristics; (e) EQE–bias characteristics; and (f) EQE–luminance characteristics.

stack, while **4c** suffers pronounced efficiency loss at high brightness. The CIE chromaticity diagram shows that **4a** emits in the deep blue region, **4b** in the sky-blue range, and **4c** shifts toward cyan, reflecting the progressive red-shift in emission from **4a** to **4c**. This trend correlates with the increasing charge-transfer (CT) character and decreasing ΔE_{ST} among the isomers. From the current density *vs.* bias curves, all devices display typical diode-like behaviour, but **4b** achieves the highest current density at a given bias, suggesting improved charge mobility or balance.

The EQE–luminance characteristics reveal efficiency roll-off at higher luminance levels for all devices, but the roll-off is less pronounced in **4b**, indicating better exciton stability and reduced triplet–triplet annihilation. Overall, the positioning of the *N*-PhCbz donor plays a pivotal role in modulating device performance, with **4b** achieving the most balanced and efficient electroluminescence due to its optimal ΔE_{ST} and multi-channel emission contributions.

Time-resolved PL reveals that none of the isomers engages a viable TADF channel: even in the more CT-stabilizing CBP host the ΔE_{ST} values remain too large for efficient RISC (*e.g.*, 0.60 eV (**4a**), 0.21 eV (**4b**), and 0.15 eV (**4c**)), and the delayed components observed optically are RTP in the millisecond regime and, in CBP, DF arising from TTA rather than TADF. Consequently, under electrical drive the emissive output lacks any triplet-harvesting contribution. The device's behaviour is explained by

very fast TTA operating on microsecond timescales under electrical excitation, which rapidly depletes the triplet population at the high exciton densities present in OLEDs, long before millisecond RTP can radiate. This assignment is consistent with classic transient-EL/kinetic analyses of OLEDs in which TTA is identified as a dominant triplet loss and, in fluorescent devices, as the source of delayed upconverted singlets ("triplet fusion"). In parallel, triplet–polaron quenching (TPQ) further suppresses long-lived triplets in working pixels: polarons present in the emission zone or at adjacent interfaces provide highly efficient non-radiative decay pathways that are competitive with, or stronger than, bulk quenching channels, thereby rendering ms-RTP invisible in EL even when it is prominent in PL. Taken together, the photophysics measured on films and the device metrics (high peak EQE with roll-off; no RTP features in EL) are self-consistent: there is no TADF, TTA in the microsecond regime dominates the triplet kinetics in devices, and polaron-induced quenching finishes off the remaining triplets, so the electroluminescence is entirely singlet based fluorescence involving TTA.

3. Conclusions

In summary, donor–acceptor positional isomers, namely **4a**, **4b** and **4c**, synthesized, characterized and found to exhibit RTP,

7462 | *J. Mater. Chem. C*, 2026, **14**, 7451–7465

This journal is © The Royal Society of Chemistry 2026

AIE, dual emission and TSCT properties. Single-crystal XRD analysis was used to determine the intramolecular and intermolecular interactions between molecules, thereby proving H-bonding and TSCT. DFT and TDDFT calculations were used to explore the electronic properties of the positional isomers (**4a**, **4b** and **4c**) in the ground and excited states to validate experimental results. Positional isomers **4a**, **4b** and **4c** showed AIE properties due to restricted intramolecular rotation governed by D–A twisting. Isomer **4b** showed dual emission due to LE and CT character, which was analyzed using a toluene/DCM binary solvent system. Isomer **4c** showed TSCT properties due to a large dihedral angle between the donor and acceptor leading to D–A proximity. Although energy gaps can be tuned substantially, the isomers do not favor ultrafast RISC, placing them outside of TADF design and instead accelerating alternative triplet utilization pathways. The OLED performance of positional isomers directly aligns these excited state photophysical trends, with **4b** achieving the most favorable balance between CT character and triplet loss suppression. Overall, this work shows that just shifting the donor position on the acceptor core can control multichannel emission and triplet exciton dynamics, and improve the device performance of organic materials.

Author contributions

K. R. Justin Thomas: conceptualization, methodology, theoretical calculations, review, editing, supervision, and funding acquisition. Przemyslaw Data: conceptualization, methodology, review, editing, supervision, and funding acquisition. Ajeet Kumar Sharma: methodology, experiments, and writing original draft. Prasannamani Govindharaj: methodology, experiments, and writing original draft.

Conflicts of interest

The authors declare no competing financial interests.

Data availability

The data supporting this article have been included as part of the supplementary information (SI). Supplementary information: experimental details, materials and instruments as well as additional characterization data including NMR spectra, UV-visible spectra, PL spectra, CHNS analysis, DSC, TGA, SEM and table showing SC-XRD analysis results of **4a**, **4b** and **4c**. See DOI: https://doi.org/10.1039/d6tc00271d.

CCDC 2516522–2516524 contain the supplementary crystallographic data for this paper.[69a–c]

Acknowledgements

References

1 T. Kim, G. Shin, T. Park and M. Kim, *Adv. Funct. Mater.*, 2025, **35**, 2412267.
2 K. Zhang, Z. Zhou, D. Liu, Y. Chen, S. Zhang, J. Pan, X. Qiao, D. Ma, S. Su, W. Zhu and Y. Liu, *Angew. Chem., Int. Ed.*, 2024, **136**, e202407502.
3 S. Banerjee, P. Singh, P. Purkayastha and S. K. Ghosh, *Chem. – Asian J.*, 2024, **20**, e202401291.
4 L. Zhu, M. Zhang, Z. Zhou, W. Zhong, T. Hao, S. Xu, R. Zeng, J. Zhuang, X. Xue, H. Jing and Y. Zhang, *Nat. Rev. Electr. Eng.*, 2024, **1**, 581.
5 N. Yang, S. Zhang, Y. Cui, J. Wang, S. Cheng and J. Hou, *Nat. Rev. Mater.*, 2025, **10**, 404.
6 K. Xue, X. Z. Zhu, J. F. Yan, S. H. Chen and Y. F. Yuan, *ChemPhotoChem*, 2025, **9**, e202500017.
7 A. Rahman, S. Bo, A. Ali, L. Zhang, S. Y. Alomer and F. Liu, *RSC Adv.*, 2024, **14**, 11350.
8 C. Si, T. Wang, Y. Xu, D. Lin, D. Sun and E. Zysman-Colman, *Nat. Commun.*, 2024, **15**, 7439.
9 E. Cha, J. Jeon, H. W. Kim, H. U. Lee, J. Y. Woo, J. S. Yeo, H. B. Kwon, S. B. Cho and T. H. Han, *Adv. Funct. Mater.*, 2025, e08146.
10 S. Roh, S. Lee, H. Ham, B. H. Jhun, H. Yee, Y. You, B. Kim and M. S. Kang, *Small Methods*, 2025, **9**, 2401719.
11 Y. Chang, K. Zhang, L. Zhao, X. Wang, S. Wang, S. Shao and L. Wang, *Angew. Chem., Int. Ed.*, 2025, **64**, e202415607.
12 M. Zhang, D. M. Sun, K. Wang, J. Chen, Y. Q. Zhou, H. Y. Zhang, H. Zhuo, Z. H. Xiong, H. Lin, S. L. Tao and C. J. Zheng, *Adv. Funct. Mater.*, 2025, **35**, 2414808.
13 T. Ishii, K. Ikeda, M. Ogawaa and Y. Kusakaki, *RSC Adv.*, 2015, **5**, 89171.
14 Y. Fu, H. Liu, B. Z. Tang and Z. Zhao, *Adv. Funct. Mater.*, 2024, **34**, 2401434.
15 U. Mitschke and P. Bäuerle, *J. Mater. Chem. A*, 2000, **10**, 1471.
16 J. Sun, H. Ahn, S. Kang, S.-B. Ko, D. Song, H. A. Um, S. Kim, Y. Lee, P. Jeon and S.-H. Hwang, *Nat. Photonics*, 2022, **16**, 212.
17 O. Bezvikonnyi, A. Bucinskas, P. Arsenyan, A. Petrenko, Z. Y. Wei, J. H. Lee, D. Volyniuk, E. U. Rashid, T. L. Chiu and J. V. Grazulevicius, *ACS Appl. Electron. Mater.*, 2024, **6**, 4489.

This journal is © The Royal Society of Chemistry 2026

J. Mater. Chem. C, 2026, **14**, 7451–7465 | **7463**

18 J. Wang, Y. Yang, F. Gu, X. Zhai, C. Yao, J. Zhang, C. Jiang and X. Xi, *ACS Appl. Mater. Interfaces*, 2023, **15**, 59643.

19 J. Wang, Y. Yang, C. Jiang, M. He, C. Yao and J. Zhang, *J. Mater. Chem. C*, 2022, **10**, 3163.

20 Y. Liu, C. Li, Z. Ren, S. Yan and M. R. Bryce, *Nat. Rev. Mater.*, 2018, **3**, 1.

21 A. K. Sharma and K. R. J. Thomas, *ChemPhotoChem*, 2025, **9**, e202500100.

22 Q. Zhang, H. Kuwabara, W. J. Potscavage Jr, S. Huang, Y. Hatae, T. Shibata and C. Adachi, *J. Am. Chem. Soc.*, 2014, **136**, 18070.

23 C. Chen, R. Huang, A. S. Batsanov, P. Pander, Y. T. Hsu, Z. Chi, F. B. Dias and M. R. Bryce, *Angew. Chem., Int. Ed.*, 2018, **130**, 16645.

24 A. B. Pun, L. M. Campos and D. N. Congreve, *J. Am. Chem. Soc.*, 2019, **141**, 3777.

25 J. Wang, Y. Niu, Y. Jiang, Z. Chen, C. Yao, W. Yao, M. He and J. Zhang, *Mater. Today Chem.*, 2025, **47**, 102796.

26 A. Ekbote, S. M. Mobin and R. Misra, *J. Mater. Chem. C*, 2020, **8**, 3589.

27 S. Zhang, Y. Huang, L. Kong, X. Zhang and J. Yang, *Dyes Pigm.*, 2020, **181**, 108574.

28 X. He and P. Wei, *Chem. Soc. Rev.*, 2024, **53**, 6636.

29 J. Mei, N. L. Leung, R. T. Kwok, J. W. Lam and B. Z. Tang, *Chem. Rev.*, 2015, **115**, 11718.

30 W. Che, Y. Gong, L. Tu, M. Han, X. Li, Y. Xie and Z. Li, *Phys. Chem. Chem. Phys.*, 2020, **22**, 21445.

31 Z. Mao, Z. Yang, C. Xu, Z. Xie, L. Jiang, F. L. Gu, J. Zhao, Y. Zhang, M. P. Aldred and Z. Chi, *Chem. Sci.*, 2019, **10**, 7352.

32 Z. Zhao, C. Zeng, X. Peng, Y. Liu, H. Zhao, L. Hua, S. J. Su, S. Yan and Z. Ren, *Angew. Chem., Int. Ed.*, 2022, **61**, e202210864.

33 S. Park, J. E. Kwon, S. H. Kim, J. Seo, K. Chung, S. Y. Park, D. J. Jang, B. M. Medina, J. Gierschner and S. Y. Park, *J. Am. Chem. Soc.*, 2009, **131**, 14043.

34 K. W. Bentley and C. Wolf, *J. Am. Chem. Soc.*, 2013, **135**, 12200.

35 S. V. Mulay, Y. Kim, M. Choi, D. Y. Lee, J. Choi, Y. Lee, S. Jon and D. G. Churchill, *Anal. Chem.*, 2018, **90**, 2648.

36 Q. Xiao, J. Zheng, M. Li, S. Z. Zhan, J. H. Wang and D. Li, *Inorg. Chem.*, 2014, **53**, 11604.

37 X. Li, S. Shen, C. Zhang, M. Liu, J. Lu and L. Zhu, *Sci. China: Chem.*, 2021, **64**, 534.

38 X. Li, G. Baryshnikov, C. Deng, X. Bao, B. Wu, Y. Zhou, H. Ågren and L. Zhu, *Nat. Commun.*, 2019, **10**, 731.

39 Z. Yang, Z. Mao, Z. Xie, Y. Zhang, S. Liu, J. Zhao, J. Xu, Z. Chi and M. P. Aldred, *Chem. Soc. Rev.*, 2017, **46**, 915.

40 A. K. Mazumdar, G. P. Nanda, N. Yadav, U. Deori, U. Acharyya, B. Sk and P. Rajamalli, *Beilstein J. Org. Chem.*, 2022, **18**, 1177.

41 Y. Xiong, J. Huang, Y. Liu, B. Xiao, B. Xu, Z. Zhao and B. Z. Tang, *J. Mater. Chem. C*, 2020, **8**, 2460.

42 Z. Yang, Y. Zhan, Z. Qiu, J. Zeng, J. Guo, S. Hu, Z. Zhao, X. Li, S. Ji, Y. Huo and S. J. Su, *ACS Appl. Mater. Interfaces*, 2020, **12**, 29528.

43 V. Thangaraji, P. Rajamalli, J. Jayakumar, M. J. Huang, Y. W. Chen and C. H. Cheng, *ACS Appl. Mater. Interfaces*, 2019, **11**, 17128.

44 T. Viswanathan, Y. Kusakabe, U. Acharyya, H. Kaji and P. Rajamalli, *ACS Appl. Opt. Mater.*, 2024, **2**, 2409.

45 A. K. Sharma, Panaha, K. R. J. Thomas, C. J. Wu, D. Luo, S. W. Liu and C. H. Chen, *Dyes Pigm.*, 2026, **248**, 113556.

46 J. Guo, X.-L. Li, H. Nie, W. Luo, R. Hu, A. Qin, Z. Zhao, S.-J. Su and B. Z. Tang, *Chem. Mater.*, 2017, **29**, 3623.

47 J. Guo, X.-L. Li, H. Nie, W. Luo, S. Gan, S. Hu, R. Hu, A. Qin, Z. Zhao, S.-J. Su and B. Z. Tang, *Adv. Funct. Mater.*, 2017, **27**, 1606458.

48 J. Huang, H. Nie, J. Zeng, Z. Zhuang, S. Gan, Y. Cai, J. Guo, S.-J. Su, Z. Zhao and B. Z. Tang, *Angew. Chem., Int. Ed.*, 2017, **56**, 12971.

49 J. A. Letizia, A. Facchetti, C. L. Stern, M. A. Ratner and T. J. Marks, *J. Am. Chem. Soc.*, 2005, **127**, 13476.

50 X. Song, Z. Liu, M. Lu, S. Zou, F. Guo, S. Gao, Z. Zhao, B. Z. Tang and Y. Zhang, *J. Mater. Chem. C*, 2022, **10**, 17550.

51 L. Zhan, Y. Xiang, Z. Chen, K. Wu, S. Gong, G. Xie and C. Yang, *J. Mater. Chem. C*, 2019, **7**, 13953.

52 Q. Li, Z. Zhao, H. Zhao, Y. Guo, X. Tong, S. Yan and Z. Ren, *ACS Appl. Mater. Interfaces*, 2024, **16**, 22238.

53 S. Cai, H. Shi, J. Li, L. Gu, Y. Ni, Z. Cheng, S. Wang, W. W. Xiong, L. Li, Z. An and W. Huang, *Adv. Mater.*, 2017, **29**, 1701244.

54 T. Lu, *J. Chem. Phys.*, 2024, **161**, 082503.

55 J. Huang, C. Li, Y. J. Xia, X. H. Zhu, J. Peng and Y. Cao, *J. Org. Chem.*, 2007, **72**, 8580.

56 Y. J. Pu, M. Higashidate, K. I. Nakayama and J. Kido, *J. Mater. Chem.*, 2008, **18**, 4183.

57 J. Huang, Q. Liu, J. H. Zou, X. H. Zhu, A. Y. Li, J. W. Li, S. Wu, J. Peng, Y. Cao, R. Xia, D. D. C. Bradley and J. Roncali, *Adv. Funct. Mater.*, 2009, **19**, 2978.

58 Q. Wei, P. Kleine, Y. Karpov, X. Qiu, H. Komber, K. Sahre, A. Kiriy, R. Lygaitis, S. Lenk, S. Reineke and B. Voit, *Adv. Funct. Mater.*, 2017, **27**, 1605051.

59 R. K. Konidena, K. R. J. Thomas, S. Kumar, Y. C. Wang, C. J. Li and J. H. Jou, *J. Org. Chem.*, 2015, **80**, 5812.

60 C. Reichardt, *Chem. Rev.*, 1994, **94**, 2319.

61 F. Bu, R. Duan, Y. Xie, Y. Yi, Q. Peng, R. Hu, A. Qin, Z. Zhao and B. Z. Tang, *Angew. Chem., Int. Ed.*, 2015, **54**, 14700.

62 C. Wu, C. Shi, Y. Zheng, J. Zhang, Y. Wang, N. Sun, Q. Wang and Z. H. Lu, *Chem. Eng. J.*, 2022, **431**, 133249.

63 A. Sharma, R. Balasaravanan, K. R. J. Thomas, M. Ram, D. K. Dubey, R. A. K. Yadav and J. H. Jou, *Dyes Pigm.*, 2021, **184**, 108830.

64 M. C. Tang, M. Y. Leung, S. L. Lai, M. Ng, M. Y. Chan and V. W. W. Yam, *J. Am. Chem. Soc.*, 2018, **140**, 13115.

65 H. Wang, H. Ma, N. Gan, K. Qin, Z. Song, A. Lv, K. Wang, W. Ye, X. Yao, C. Zhou and X. Wang, *Nat. Commun.*, 2024, **15**, 2134.

66 S. J. Zheng, J. Ma, J. Su, P. I. Djurovich, M. E. Thompson and T. Y. Li, *J. Am. Chem. Soc.*, 2024, **146**, 19042.

7464 | *J. Mater. Chem. C*, 2026, **14**, 7451–7465

This journal is © The Royal Society of Chemistry 2026

67 G. Q. Huang, R. Q. Xia, X. Chen, H. Yang, Y. L. Huang, K. Wu, J. Zheng, W. Lu and D. Li, *J. Am. Chem. Soc.*, 2025, **147**, 6415.

68 P. Li, Z. Chen, M. Y. Leung, S. L. Lai, S. C. Cheng, W. K. Kwok, C. C. Ko, M. Y. Chan and V. W. W. Yam, *J. Am. Chem. Soc.*, 2025, **147**, 12092.

69 (*a*) CCDC 2516522: Experimental Crystal Structure Determination, 2026, DOI: 10.5517/ccdc.csd.cc2qgn40; (*b*) CCDC 2516523: Experimental Crystal Structure Determination, 2026, DOI: 10.5517/ccdc.csd.cc2qgn51; (*c*) CCDC 2516524: Experimental Crystal Structure Determination, 2026, DOI: 10.5517/ccdc.csd.cc2qgn62.